SUBMITTED TO ApJ 2003 MARCH 20
Preprint typeset using LaTeX style emulateapj v. 11/12/01

THE SPECTRA OF T DWARFS. II. RED OPTICAL DATA

ADAM J. BURGASSER[1,2], J. DAVY KIRKPATRICK[3], JAMES LIEBERT[4], AND ADAM BURROWS[4]
Submitted to ApJ 2003 March 20

ABSTRACT

We present 6300–10100 Å spectra for a sample of 13 T dwarfs observed using LRIS mounted on the Keck 10m Telescope. A variety of features are identified and analyzed, including pressure-broadened K I and Na I doublets; narrow Cs I and Rb I lines; weak CaH, CrH, and FeH bands; strong H_2O absorption; and a possible weak CH_4 band. Hα emission is detected in three of the T dwarfs, strong in the previously reported active T dwarf 2MASS 1237+6526 and weak in SDSS 1254−0122 and 2MASS 1047+2124. None of the T dwarfs exhibit Li I absorption. Guided by the evolution of optical spectral features with near-infrared spectral type, we derive a parallel optical classification scheme spanning L8 to T8, anchored to select spectral standards. We find general agreement between optical and near-infrared types for nearly all of the T dwarfs so far observed, within our classification uncertainties (∼1 subtype). These results suggest that competing gravity and temperature effects compensate for each other over the 0.6–2.5 μm spectral region. We identify one possible means of disentangling these effects by comparing the strength of the K I red wing to the 9250 Å H_2O band. One of our objects, 2MASS 0937+2931, exhibits a peculiar spectrum, with a substantial red slope and relatively strong FeH absorption, both consequences of a metal-deficient atmosphere. Based on its near-infrared properties and substantial space motion, this object may be a thick disk or halo brown dwarf.

Subject headings: stars: activity — stars: fundamental parameters — stars: individual (2MASS J09373487+2931409) stars: low mass, brown dwarfs

1. INTRODUCTION

Current classification schemes for the two latest spectral classes, L dwarfs (Kirkpatrick et al. 1999; Martín et al. 1999) and T dwarfs (Burgasser et al. 2002c; Geballe et al. 2002), are defined in different spectral regions. L dwarf classification is tied to the red optical region (6300–10000 Å), enabling straightforward comparison with M dwarf classification schemes (Kirkpatrick, Henry, & McCarthy 1991), and hence a well-defined demarcation of the M and L spectral classes. T dwarf classification is tied to the near-infrared region (1–2.5 μm), taking advantage of both greater relative brightness (∼ 75% of the emergent flux) and the presence of strong H_2O and defining CH_4 bands. Classifications in different spectral regions cannot be expected to be identical due to the competing influences of temperature, gravity, and composition at different wavelengths. This may be especially true for late-type M, L, and T dwarfs, whose molecular-rich atmospheres also contain condensate clouds, predominantly affecting near-infrared spectral flux (Tsuji, Ohnaka, & Aoki 1999; Ackerman & Marley 2001). The influence of these chemical and physical variables muddle the characterization of the L/T transition, a spectromorphological boundary that encompasses a dramatic shift in near-infrared colors (J–K $\approx 2 \rightarrow 0$), condensate opacity, and overall spectral energy distribution. Clearly, the evolution of both near-infrared and optical spectra must be examined to fully characterize this critical transition.

The red optical spectra of T dwarfs are of interest in their own right, as they encompass unique features and diagnostics of physical parameters. Early investigation of the prototype of this class, Gliese 229B (Nakajima et al. 1995; Oppenheimer et al. 1995), revealed strong H_2O and weak CH_4 molecular absorption (counterparts to the strong bands that dominate the near-infrared spectrum), Cs I alkali lines, and a steep red spectral slope shortward of 1 μm (Oppenheimer et al. 1998; Shultz et al. 1998). The latter feature, attributable to the pressure-broadened wings of the 7665/7699 Å K I resonant doublet lines (Tsuji, Ohnaka, & Aoki 1999; Liebert et al. 2000; Burrows, Marley, & Sharp 2000), is responsible for the extremely red optical/near-infrared colors of this object (R–J ∼ 9.1; Matthews et al. 1996, Golimowski et al. 1998), a property that has been exploited in the search for T dwarfs in wide-field surveys such as the Two Micron All Sky Survey (Skrutskie et al. 1997, hereafter 2MASS) and the Sloan Digital Sky Survey (York et al. 2000, hereafter SDSS). Burrows et al. (2002a) have shown that these heavily-broadened lines and their 5890/5896 Å Na I counterparts are sensitive to both effective temperature (T_{eff}) and specific gravity. The much weaker Cs I lines are key tracers of atmospheric rainout (Griffith & Yelle 1999; Lodders 1999). Additional molecular bands of FeH and CrH reported in the spectra of mid-type T dwarfs (Burgasser et al. 2000a) are possible tracers of condensate cloud opacity across the L/T transition (Burgasser et al. 2002b). Finally, persistent Hα emission detected in the T dwarf 2MASS 1237+6526 (Burgasser et al. 2000a, 2002a), whose atmosphere should be too cool to support a substantial chromosphere (Mohanty et al. 2002; Gelino et al. 2002), is not

[1] Department of Astronomy & Astrophysics, University of California at Los Angeles, Los Angeles, CA, 90095-1562; adam@astro.ucla.edu
[2] Hubble Fellow
[3] Infrared Processing and Analysis Center, M/S 100-22, California Institute of Technology, Pasadena, CA 91125; davy@ipac.caltech.edu
[4] Steward Observatory, University of Arizona, Tucson, AZ 85721; liebert@as.arizona.edu, burrows@as.arizona.edu

yet understood and has been the subject of some debate (Hall 2002a,b; Liebert et al. 2003).

In this article, we continue the spectroscopic investigation of T dwarfs initiated in Burgasser et al. (2002c, Paper I) by examining their red optical spectra. This article compliments that of Kirkpatrick et al. (2003), which discusses the optical L/T transition in detail. In §2 we describe the acquisition and reduction of the data, obtained with the Low Resolution Imaging Spectrograph (Oke et al. 1995, hereafter LRIS) mounted on the Keck 10m Telescope. In §3 we present the reduced spectra, analyzing in detail the spectral features observed. In §4 we present a classification scheme for T dwarfs using red optical spectra that is parallel to but independent of the near-infrared scheme of Burgasser et al. (2002c). In §5 we discuss our results, including the physical properties of the peculiar T dwarf 2MASS 0937+2931, a possible means of disentangling gravity and temperature in red optical spectra, and a comparison between T dwarf optical and near-infrared classifications. We summarize our results in §6.

2. OBSERVATIONS

We acquired LRIS red optical spectra for a sample of 13 T dwarfs identified in 2MASS (Burgasser et al. 1999, 2000b,c, 2002c, 2003a) and SDSS (Leggett et al. 2000) on three nights, 2000 March 5, 2001 February 20, and 2003 January 2 (UT). An observing log is given in Table 1. Conditions during our March 2000 and January 2003 observations were clear with seeing $\lesssim 1''$; our February 2001 observations were made through light clouds with $1''$ seeing. LRIS is nominally a dual spectrograph with a 5500 Å dichroic mirror separating incoming light into two (red and blue) channels; however, for all observations we used only the red channel with a mirror bypassing the dichroic. The OG570 order-blocking filter was employed to suppress higher-order light, and a $1''$ (4.7 pixels) slit was used with the 400 lines mm^{-1} grating blazed at 8500 Å, yielding 6300–10100 Å spectra with ~7 Å resolution (R ~ 1200). Dispersion on the chip was 1.9 Å $pixel^{-1}$.

Targets were nominally acquired using the facility guide camera; objects that were too optically faint to be seen in the guider image were placed into the slit by blind offset from a nearby visible source, using offset values determined from 2MASS coordinates. Individual exposures ranged from 1200 to 1800 sec, with up to four observations obtained on a particular night. Observations of the B1 V flux standard Hiltner 600 (Hamuy et al. 1994) were obtained for flux calibration on all runs using the same instrumental configuration. To correct for telluric absorption, we observed either DA/DC/DZ white dwarfs selected from McCook & Sion (1999) or late-F/early-G stars before or after the target observations and at similar airmass. These stars typically have few or no features in the red optical telluric absorption bands. Quartz lamp flat-field exposures (reflected off of the interior dome) were observed at the start of each run to calibrate detector response, and NeAr arc lamp exposures were obtained immediately after the target observations for wavelength calibration.

Science data were reduced using standard IRAF[5] routines. First, we removed the image bias. For the March 2000 data, this was done by median-combining a series of one-second bias frames, and subtracting this image from the science and calibration data. For the February 2001 and January 2003 data, the bias level for each row was derived from the mean counts in the overscan region and subtracted. Images were trimmed and divided by the median-combined and normalized flat-field exposures to correct for detector response. Spectra were then extracted using the IRAF APEXTRACT package. Curvature of the dispersion line was determined from either the telluric or flux standard star exposures and used as a template for the target extractions. All spectral data were optimally extracted with a cleaning algorithm to eliminate cosmic rays and spurious pixels. Wavelength calibration was done using the arc lamp exposures and line identifications from the NIST atomic line database[6].

We then computed a telluric correction from the telluric calibrator spectra by interpolating over atmospheric O_2 (~6850–6900 Å B-band, ~7600–7700 Å A-band) and H_2O (~7150–7300, ~8150–8350, and ~8950–9650 Å; Stevenson 1994) bands, and then dividing this modified spectrum by the original calibrator spectrum. This correction spectrum was applied to both target and flux standard data to eliminate telluric absorption from the spectrum[7] We note that we acquired the wrong star as the telluric calibrator for 2MASS 0937+2931. WD 0924+199 (a.k.a PG 0924+199, TON 1061) is classified DC5 (Putney 1997), with a possible indication of Hα absorption and an 11,000 K blackbody continuum. Our observations show a roughly 5000 K blackbody continuum, weak and narrow Hα absorption, a strong Ca II resonance triplet (8498, 8542, & 8662 Å) and a Ba II line at 6497 Å. This object is likely a background F/G-type dwarf, and fortuitously works fine as a telluric calibrator[8].

Finally, flux calibration was done by correcting our Hiltner 600 observations to the spectrophotometric data given by Hamuy et al. (1994), being careful to interpolate over telluric absorption regions and the Balmer Hα line. This correction was applied to the T dwarf data to produce the final calibrated spectra. If multiple spectra were obtained on a particular night, these were coadded with a sigma-clipping algorithm to improve signal-to-noise.

3. THE SPECTRA

Reduced spectra for the T dwarfs are shown in Figure 1 in order of their near-infrared spectral classifications. Fea-

[5] Image Reduction and Analysis Facility (IRAF) is distributed by the National Optical Astronomy Observatories, which are operated by the Association of Universities for Research in Astronomy, Inc., under cooperative agreement with the National Science Foundation.

[6] See http://physics.nist.gov/.

[7] Telluric corrections were applied to the flux standard for the March 2000 data only, as the February 2001 and January 2003 data were first flux calibrated, then corrected for telluric absorption. Reversing the order of these corrections has a negligible affect on the resulting science data.

[8] We also detected the Ca II resonance triplet in the DZA5 WD 1225-079 (a.k.a. PG 1225-079, K 789-37), which is known to have strong Ca II HK absorption at 3933 and 3968 Å (Liebert, Wehrse, & Green 1987). WD 0552-041 (a.k.a. HL 4, LHS 32), variously classified from DC9 to DZ11.5 (McCook & Sion 1999) shows no metal lines in its red optical spectrum, consistent with a pure He atmosphere. See Harris et al. (2003) for additional discussion of the red optical spectra of white dwarfs.

tures present in the spectra are noted in Figure 1 and listed in Table 2; we discuss these features in detail below.

3.1. *Atomic Line Features*

The strongly pressure-broadened Na I and K I resonance doublets suppress most of the optical flux of T dwarfs (Burrows et al. 2002a). The broad wings of both alkali doublets can be seen clearly in the highest signal-to-noise spectrum of our sample, that of 2MASS 0559−1404, shown in Figure 2 with absolute flux density (calibrated using I_c photometry and parallax measurements from Dahn et al. 2002) plotted on a logarithmic scale. The peak-up in flux between these features is clearly evident, and their shapes are consistent with heavily pressure-broadened atomic lines (Burrows & Volobuyev 2003).

Other alkali line features present in these spectra include the 8521/8943 Å Cs I and 7800/7948 Å Rb I resonant doublets. Examination of Figure 1 shows that the Cs I lines are clearly present in all of the T dwarfs observed, although they become rather weak in that latest-type objects. Rb I lines lie very close to the core of the strong K I doublet, and are generally only seen in our higher signal-to-noise spectra (e.g., Figure 2).

We have measured pseudo-equivalent widths[9] (pEWs) for each of the Cs I and Rb I lines as follows: First, we subtracted a linear fit to the local pseudo-continuum, $C(\lambda)$, to yield the line profile, $L(\lambda)$. Next, we fit each line profile to a Gaussian function of the form

$$L(\lambda) = Ae^{-\frac{1}{2}(\frac{\lambda-\lambda_c}{\Delta\lambda})^2}, \quad (1)$$

where A, λ_c (the transition wavelength in Å), and $\Delta\lambda$ (the line width in Å) were left as free parameters. We found that Gaussian profiles were generally superior to Lorentzian profiles due to oversampling of the instrumental spectral resolution on the chip. Finally, pseudo-equivalent widths were derived from

$$pEW = -\frac{\sqrt{2\pi}A\Delta\lambda}{C(\lambda_c)}. \quad (2)$$

Uncertainties, or upper limits in the case where no line could be visually identified, were derived from the mean of pEWs from neighboring noise spikes. Values are listed in Table 3.

Early- and mid-type T dwarfs have Cs I pEWs of 4.0–7.4 Å, with the 8521 Å line weakening rapidly in the later-type objects; 2MASS 0415−0935 shows the weakest 8521 Å line with a pEW = 1.5±0.9 Å. Pseudo-equivalent widths for the 8943 Å line also generally decrease in the later-type T dwarfs, but not as significantly as the 8521 Å line, possibly the result of contamination by CH_4 absorption (§3.2; Figure 4). These trends are consistent with chemical equilibrium calculations by Lodders (1999), which predict a gradual chemical depletion of Cs to CsCl at T $\lesssim$ 1300 K, accelerated at T $\lesssim$ 1000 K as NaCl (and atomic Na) converts to Na_2S and liberates elemental Cl. Note that K is depleted to KCl around the same temperature (Lodders 1999), weakening the K I wing and reducing the suppression of the local pseudo-continuum around the Cs I lines. That the Cs I lines nevertheless wane in the later T dwarfs provides supporting evidence that elemental Cs is in fact depleted in their photospheres.

The 7948 Å Rb I line could be measured in about half of the objects in our sample, surprisingly in many of the latest-type T dwarfs. However, pEWs for the latter have large uncertainties and may be overestimated due to the weak continuum in this spectral region. Figure 3 shows a close-up around the 7948 Å line for five T dwarfs with positive detections; for 2MASS 0727+1710, Gliese 570D, and 2MASS 0415−0935, these detections are clearly marginal. Nonetheless, the resurgence of the Rb I line could be a real effect. As with K, atomic Rb is depleted to RbCl for T $\lesssim$ 1000 K (Lodders 1999). The lower depletion temperature for Rb implies a much higher relative abundance than Cs in the later T dwarfs, particularly as Rb is roughly 20 times more abundant in a Solar metallicity mixture (Anders & Grevesse 1989). Furthermore, the weakening of the K I red wing is likely to enhance Rb I pEWs. Unfortunately, the proximity of the Rb I lines to the center of K I resonance doublet inhibits their detection in all but the highest signal-to-noise spectra. The 7800 Å Rb I line is only detected in our three brightest T dwarfs, 2MASS 0559−1404, SDSS 1254−0122, and 2MASS 1503+2525, with strengths of 4.2±1.9, 6±3, and 10±2 Å, respectively.

One glaring absence among the alkali features is the 6708 Å Li I resonance doublet. 2MASS 0559−1404 shows a possible feature close to this line (Figure 2), but it is offset at 6690 Å and is likely a residual noise spike. All of the objects in our sample are presumably substellar based on their low T_{eff}s (Burrows et al. 1997; Burgasser et al. 2002c), and a good fraction likely have masses below the 0.06 $M_\odot$ limit for Li core fusion depletion (Chabrier & Baraffe 1997). However, none exhibit Li I absorption. Atomic Li is chemically depleted to LiCl, LiH, and LiOH for T $\lesssim$ 1500 (Lodders 1999), at hotter temperatures than Na, K, Rb, and Cs. A general weakening of the Li I line is observed in substellar late-type L dwarfs (Kirkpatrick et al. 2000), and the absence of this line in the T dwarfs is consistent with a temperature effect. However, we note that these observations are not consistent with current spectral models using the Lodders (1999) chemical abundances, which continue to exhibit detectable Li I absorption down to $T_{eff} \approx$ 600–800 K (Allard et al. 2001; Burrows et al. 2002a). Confirmation of chemical depletion of all of the alkali species will require examination of their respective chloride bands at far-infrared wavelengths.

3.2. *Molecular Features*

The most prominent molecular features in the red optical spectra of T dwarfs are the H_2O bands at 9250 and 9450 Å. These bands strengthen considerably toward the latest-type objects in our sample, but are generally weaker than their near-infrared counterparts. As is the case in the near-infrared, the steam bands overlap telluric H_2O absorption at 8950–9700 Å (strongest from 9300–9650 Å; Stevenson 1994); however, the hotter brown dwarf bands clearly extend blueward to 9250 Å.

The 9896 Å Wing-Ford FeH band is seen quite clearly in many of the spectra of Figure 1; Figure 2 of Burgasser et al. (2002b) shows a close-up of this feature and the 9969 Å CrH band. Both bands are strongest in mid-type T

[9] The presence of overlying opacity from K I, Na I, and other species prevents the measurement of "true continuum" for computing equivalent widths; hence, the reported measurements are relative to the local "pseudo-continuum".

dwarfs like 2MASS 1534−2952AB, but are weak or absent in the latest-type T dwarfs. The identification of the CrH band may be in error, as Cushing et al. (2003) find that absorption in this region for M and L dwarfs is entirely attributable to FeH absorption. While opacity data from Burrows et al. (2002b) clearly show a CrH bandhead at this wavelength, its visibility depends on the relative abundance of CrH to FeH, as their opacities are roughly equal in strength at these wavelengths (Dulick et al. 2003). Lodders (1999) predicts an equilibrium abundance CrH/FeH $\approx 10^{-3}$ for $1800 \lesssim T \lesssim 2500$ K, but a higher relative abundance of roughly 0.3 for $T \lesssim 1500$ K. Hence, it is entirely possible for the 9969 Å CrH band to be overwhelmed by FeH absorption in M and L dwarf spectra, but detectable in the cooler T dwarf spectra. Higher-resolution observations are required to test this possibility. The shorter-wavelength counterparts of the FeH and CrH bands at 8692 and 8611 Å, respectively, are present in the spectrum of SDSS 1254−0122, but absent in the remaining spectra.

A weak signature of CaH at 6750–7150 Å, seen in M and L dwarf spectra, also appears to be present but weak in the spectra of 2MASS 0559−1404 (Figure 2), SDSS 1254−0122, and 2MASS 1503+2525, and is not seen in any of the other spectra. In chemical equilibrium, CaH and elemental Ca are expected to be depleted to the solid minerals perovskite ($CaTiO_3$), grossite ($CaAl_2O_4$), hibonite ($CaAl_{12}O_{19}$), and gehlenite ($Ca_2Al_2SiO_7$) at $T \lesssim 1900$ K (Lodders 1999). The detection of this weak band in mid-type T dwarfs is therefore unexpected and may be indicative of non-equilibrium processes. However, improved opacities for CaH are needed before this scenario can be properly explored.

While CH_4 is ubiquitous in the near-infrared spectra of T dwarfs, only the relatively weak 8950 Å CH_4 band, noted by Oppenheimer et al. (1998) in Gliese 229B, is likely to be present in the red optical spectra of the latest-type T dwarfs. Figure 4 shows a close-up of this spectral region for six T dwarfs including Gliese 229B. Absorption at the base of the 8943 Å Cs I line clearly becomes very broad in the later-type objects, and is strongest in 2MASS 0415−0935. The shape of this feature is not typical of pressure-broadened line wings (Burrows & Volobuyev 2003); furthermore, Cs I lines weaken in the latest-type T dwarfs. Below the spectra we plot a CH_4 opacity spectrum generated from the HITRAN database (Rothman et al. 1998, see references in Burrows et al. 1997). While the broad trough around the Cs I line, and a weak feature at 8835 Å in the spectrum of 2MASS 0415−0935, are generally consistent with the CH_4 opacity data, none of the T dwarf spectra, including that of Gliese 229B, show the strong Q branch at 8875 Å. However, the CH_4 opacity data is based on laboratory measurements obtained at temperatures significantly below those of T dwarf photospheres; hence, the overall band shape may be somewhat different. Pending improved opacity data, we consider the detection of CH_4 at 8950 Å to be tentative. Three other CH_4 features at 7300, 8000, and 10000 Å seen in planetary and laboratory spectra (Dick & Fink 1977) are intrinsically weaker than the 8950 Å band and are not seen in the T dwarf data.

3.3. *Hα Emission*

Hα emission at 6563 Å is detected in three objects in our sample: 2MASS 1047+2124, 2MASS 1237+6526 (previously reported in Burgasser et al. 2000a), and SDSS 1254−0122. Figure 5 shows a close-up of the Hα spectral region for these three objects. Note that the emission lines in 2MASS 1047+2124 and SDSS 1254−0122 are very weak, detected at the 2.2 and 3σ levels, respectively, while the emission in 2MASS 1237+6526 is substantial. None of the other T dwarfs exhibit discernible emission at 6563 Å.

Emission fluxes and 3σ upper limits are listed in Table 4, along with $\log L_{H\alpha}/L_{bol}$ estimates, calculated from 2MASS J-band magnitudes and using a linear interpolation of the J-band bolometric correction as a function of near-infrared spectral type,

$$BC_J = M_{bol} - M_J = 2.97 - 0.11 \times SpT, \qquad (3)$$

(SpT(T5) = 5, etc.). This relation is based on luminosity estimates for 2MASS 0559−1404 (Burgasser 2002, $BC_J = 2.43 \pm 0.07$), Gliese 229B (Leggett et al. 1999, $BC_J = 2.19 \pm 0.10$), and Gliese 570D (Geballe et al. 2001, $BC_J = 2.09 \pm 0.10$). For SDSS 1254−0122, we used an average BC_J between 2MASS 0559−1404 and the latest-type L dwarfs (Reid et al. 2001, $BC_J \approx 1.6$). Note that pEW measurements of the Hα line is prohibited in most of these objects by the absence of a detected continuum.

At first glance, the detection of Hα emission in three T dwarfs appears to stand contrary to the reduced ionization fractions predicted in their very cool atmospheres (Mohanty et al. 2002; Gelino et al. 2002). The lack of ionized material prevents the coupling of magnetic field lines to the upper atmosphere, thereby discouraging the formation of a substantial chromosphere via collisional heating (Mohanty et al. 2002). However, the relative emission luminosity of 2MASS 1047+2124 and SDSS 1254−0122 is roughly 2 orders of magnitude lower than that of active mid-type M dwarfs, where $\log L_{H\alpha}/L_{bol}$ saturates at roughly −3.5 (Hawley, Gizis, & Reid 1996), and is substantially lower than that of active L dwarfs (Gizis et al. 2000), as shown in Figure 3 of Burgasser et al. (2002a). Hence, the emission in these objects is consistent with a reduced, though not diminished, chromosphere. The strong, persistent emission in 2MASS 1237+6526 is discussed in further detail in Burgasser et al. (2002a).

One other emission feature at 7740 Å is detected in the spectrum of 2MASS 0755+2212, noted in Figure 1. As described in Burgasser et al. (2002c), this object is aligned with a background galaxy, and the observed emission line is consistent with Hα redshifted to $z = 0.18$. The background galaxy also contributes continuum flux in the blue portion of the spectrum of 2MASS 0755+2212.

4. CLASSIFICATION OF T DWARFS IN THE RED OPTICAL

The spectral features described above show clear trends with near-infrared spectral type: an increasing spectral slope and strengthening H_2O absorption; a peak in the Cs I line strengths in the early-/mid-type T dwarfs; loss of FeH and CrH absorptions at 8692 and 8611 Å in the early-type T dwarfs, and at 9896 and 9969 Å in the late-type T dwarfs; and the possible emergence of CH_4 at 8950 Å in the latest-type T dwarfs. Hence, the makings of a spectral sequence in the red optical that parallels the near-infrared sequence are apparent.

The low signal-to-noise in most of these spectra implies that a detailed scheme is generally not possible. We have therefore aimed at deriving a rough classification that parallels the near-infrared scheme, enabling a general comparison between near-infrared and optical spectromorphologies. We stress that our optical scheme is based entirely on red optical features, and that we have no *a priori* expectation that the near-infrared and optical spectral morphologies must necessarily coincide. We have augmented our spectral sample with T dwarf LRIS data from Burgasser et al. (2000a) and Kirkpatrick et al. (2003). All of the spectra in our sample have therefore been acquired and reduced in an identical manner (with the exception of telluric absorption correction) and can therefore be reliably compared.

4.1. *Spectral Standards*

Our procedures for classification followed the basic tenets of the MK method (Morgan & Keenan 1973). We chose four T dwarfs – SDSS 1254−0122 (T2), 2MASS 0559−1404 (T5), SDSS 1624+0029 (T6), and 2MASS 0415−0935 (T8) – and the L8 2MASS 1632+1904 (Kirkpatrick et al. 1999) as our spectral standards. Three of the T dwarfs are near-infrared standards in the Burgasser et al. (2002c) classification scheme, while SDSS 1624+0029 replaces the T6 near-infrared standard 2MASS 1225−2739AB, which has been identified as an unequal-magnitude binary (Burgasser et al. 2003b). Note that the spectra of 2MASS 1632+1904 and SDSS 1624+0029 have not been corrected for telluric absorption. To improve the signal-to-noise of the spectra of SDSS 1254−0122 and 2MASS 0415−0935, we combined our data with those of Kirkpatrick et al. (2003). We did not use the T1 and T3 near-infrared standards SDSS 0837−0000 and SDSS 1021−0304 because of their low signal-to-noise data. Placeholders for the unassigned intermediate subtypes (T0, T1, T3, T4, and T7) were left to allow a consistent comparison with near-infrared classifications. To avoid confusion, we hereafter designate near-infrared and optical classifications as T_n and T_o, respectively.

All of the spectral standards are plotted together in Figure 6 in both linear and logarithmic scales. The trends discussed above are readily apparent over this short sequence. More importantly, the various standards are clearly distinguishable, and hence represent distinct spectromorphological classes. In other words, the selected standards would have been chosen to represent separate optical classes regardless of their near-infrared types.

4.2. *Classification by Visual Comparison*

Classification of the remaining spectra in our sample was first done by visual comparison to the spectral standards. We have found that the optimal means of doing this is by comparison on a logarithmic scale (e.g., right panel in Figure 6). This method permits simultaneous examination of spectral slopes ranging over two orders of magnitude in flux density with weaker molecular and atomic features. We have made visual classifications for all objects with LRIS spectra previously typed T_n0 or later; values are listed in Table 7.

In general, visual types for the T dwarfs correspond well with the near-infrared classifications given our coarse sampling. Exceptions include SDSS 0423−0414, which has an earlier-type spectral morphology than our L8 standard; Kirkpatrick et al. (2003), who classify this object as L7.5 in the optical, discusses this mismatch in detail. 2MASS 0937+2931 is assigned a peculiar visual classification because of its extreme red spectral slope, far in excess of any of the standards. We discuss this object in further detail in §5.2.

4.3. *Classification by Spectral Indices*

A more quantitative approach to classification is through the use of spectral indices, ratios of flux or flux density that measure the strengths of particular absorption or pseudo-continuum features. We examined the behavior of 20 indices sampling the Cs I, FeH, CrH, H_2O, and spectral slope features on our T dwarf spectra. Some of these were taken from the literature, possibly modified (Kirkpatrick et al. 1999; Martín et al. 1999; Geballe et al. 2002; Burrows et al. 2002a), and some are of our own construction. The most useful indices are those that show the clearest trends and greatest contrast with spectral type in the standards. All of the indices were compared, and those that best satisfied these criteria were chosen.

Eight promising indices were identified, defined in Table 5. The Cs I indices are identical to those defined by Kirkpatrick et al. (1999), measuring the strengths of the 8521 and 8943 Å Cs I lines, respectively. These indices peak around T_o2, then weaken toward the later subclasses, consistent with the behavior of the corresponding pEWs. The H_2O index samples the 9250 Å band and may be weakly affected by telluric absorption, although it has been defined to avoid the strongest absorption longward of 9300 Å (Stevenson 1994). This index increases dramatically beyond type T_o2. The FeH-a and CrH-a indices measure the shorter wavelength bands, which disappear around type T_o2, after which these indices essentially measure a limited range of spectral slope. The FeH-b and CrH-b indices measure the longer wavelength bands, and show rather complex behavior, weakening in the late L and early T dwarfs, strengthening again in the mid-type T dwarfs, and finally weakening in the late T dwarfs. Burgasser et al. (2002b) have proposed that this trend is attributable to the disruption of clouds across the L/T transition. Their complex behavior limits the use of the FeH-b and CrH-b indices to spectral types T_o5 and later. Finally, the Color-e index measures the red spectral slope due to K I absorption, but is defined at longer wavelengths than the Color-d (Kirkpatrick et al. 1999) or PC3 (Martín, Rebolo, & Zapatero Osorio 1996) indices because of the absence of detectable flux shortward of 8000 Å in many of the spectra. This index is useful earlier than type T_o2, but appears to saturate in the mid- and late-type T dwarfs, possibly due to a turnover in the strength of the K I red wing (however, see §5.2). Taking into account similar behavior between pairs of indices and differing sensitivity for early and late T types, we chose to use the Cs-a, FeH-b, Color-e, and the hybrid CrH-a/H_2O ratios for our classification. These ratio values are plotted versus optical type in Figure 7.

Ratio values for the five spectral standards are listed in Table 6, and values for the remaining T dwarf spectra in our sample, as well as the associated standard types for each ratio, are listed in Table 7. Final classifications

were derived by averaging those ratio types (FeH-b was not used for types earlier than T_o5, and Color-e was not used for types later than T_o2) and rounding off to the nearest whole subclass. Individual ratio types for each object agree within roughly one standard class. Note that SDSS 0837−0000 and SDSS 1021−0304 are assigned uncertain classifications because of the substantial gaps between the nearest standard subclasses. With the exception of these two objects, all of our spectral ratio-derived classifications agree with our visually-derived classifications within one subclass, implying that our suite of indices accurately represent the overall spectral morphology. Furthermore, their is excellent agreement between the optical ratio classifications and the near-infrared classifications, again with the exception of SDSS 0423−0414.

Based on these results, we conclude that classification of mid- and late-type T dwarfs in the optical is possible, either by visual comparison to the selected standards or through the use of spectral indices defined in Table 5. However, our scheme is only accurate to within one subclass, and is therefore not as concise as current near-infrared schemes. It appears evident that the Color-e and CrH-a/H_2O indices can cleanly delineate early-type T dwarfs in the optical, suggesting that a clear segregation of L and T dwarfs at these wavelengths is possible. However, disagreement between the optical and near-infrared spectromorphologies of the key transition object, SDSS 0423−0414, points to possible difficulties in this regime (Kirkpatrick et al. 2003). We note that none of the L dwarfs classified as L8 by Kirkpatrick et al. (1999, 2000) appear to be significantly later than 2MASS 1632+1904, consistent with the conclusion of Kirkpatrick et al. (2003) that a significant gap in optical spectromorphology remains between these two classes. Clearly, additional early-type T dwarfs need to be identified in order to fully characterize the L/T transition.

5. DISCUSSION

5.1. *2MASS 0937+2931: A Metal-Poor Halo/Thick Disk Brown Dwarf?*

The only object in our sample whose red optical spectrum appears to be clearly unique in comparison to the spectral standards is the T_n6p/T_o7p 2MASS 0937+2931. This object stands out in the near-infrared because of its enhanced CIA H_2 absorption (resulting in a highly suppressed K-band peak) and absence of the 1.25 μm K I lines, both of which point to a metal-poor or high gravity atmosphere (Burgasser et al. 2002c). As noted in § 4.2, the optical spectrum is peculiar because of its strong spectral slope, also a consequence of both low atmospheric metallicity and/or high surface gravity (Burrows et al. 2002a).

To examine the relative contribution of these secondary effects, we have compared the spectrum of 2MASS 0937+2931 to theoretical models from Burrows et al. (2002a). These models do not incorporate the most recent line broadening theory of Burrows & Volobuyev (2003), nor do they include FeH absorption, a relatively strong feature in the spectrum of 2MASS 0937+2931. Nevertheless, as the current state of the art, they serve to illustrate general trends. As discussed in Burrows et al. (2002a), increased surface gravity and decreased metallicity both result in a higher pressure photosphere, and hence enhancement of the pressure-sensitive K I and Na I line wings. This effect is strong enough to overcome the reduced column depth and decreased chemical abundance resulting from a higher gravity or lower metallicity atmosphere, respectively, which tend to weaken other chemical features, such as the 9250 Å H_2O band. Decreased temperature also strengthens the Na I and K I lines, but results in stronger H_2O bands as well (see § 5.2). When we compare these trends to the optical spectrum of 2MASS 0937+2931 (Figure 8), it becomes clear that the relatively weak H_2O band seen in these data requires a relatively high T_{eff}, while the strong Na I and K I require both a high gravity and low metallicity atmosphere. The best fitting models from Burrows et al. (2002a), T_{eff} = 800 and 1000 K, g = 3×10^5 cm s^{-2}, and $Z = 0.3Z_\odot$ are shown in Figure 8 along with the observed spectrum. Both models show somewhat stronger inner K I wings than the data, consistent with the analysis of Burrows & Volobuyev (2003) that the line-broadening theory used in Burrows et al. (2002a) overestimates the line opacity by as much as a factor of 10 shortward of 9000 Å. Nevertheless, the reasonable fit of the models to the data are indicative of a low metallicity, high gravity atmosphere. Note that the constraint on T_{eff} is fairly weak; a robust estimate could be obtained by a measurement of this object's parallax.

The substantial proper motion of 2MASS 0937+2931 (μ = 1.″4±0.″2; Burgasser et al. 2003a) suggests that it is either quite close to the Sun or has a high space velocity. (Burgasser et al. 2003a) have estimated a J-band spectrophotometric distance of roughly 9 pc, implying v_{tan} ≈ 60 km s^{-1}, which suggests (but does not guarantee) membership in the Galactic thick disk or halo populations. Such an object would have both a high surface gravity (as it must be both old and therefore more massive for its temperature) and a metal-deficient atmosphere (Gizis 1997). Burgasser et al. (2003c) have recently identified an L-type metal-deficient dwarf which, like 2MASS 0937+2931, exhibits strong K I and metal hydride absorption, relatively blue near-infrared colors, and substantial space motion. Determining whether 2MASS 0937+2931 is a cool analog to this substellar subdwarf requires additional astrometric data and refined spectral models. Nonetheless, the observed peculiarities in its optical and near-infrared spectra clearly indicate that 2MASS 0937+2931 is a unique T dwarf.

5.2. *Disentangling Gravity and Temperature Effects in T Dwarf Optical Spectra*

If we ignore metallicity variations (i.e., excluding 2MASS 0937+2931), then differences amongst the spectra in our sample are determined largely by temperature and gravity effects. The Na I and K I resonant doublet lines, which generally dominate this spectral region, are highly sensitive to both parameters. So too is the 9250 Å H_2O band. However, while the alkali lines strengthen with increased gravity, H_2O absorption decreases because of the reduced column depth of the atmosphere (Burrows et al. 2002a). The contrary behavior of these features suggests that they may be used to distinguish temperature and gravity effects in T dwarf spectra. As our sample likely includes objects with ages 0.6–3.0 Gyr (typical for the field) and 700 $\lesssim T_{eff} \lesssim$ 1200 K (Burgasser et al. 2002c), and

hence surface gravities spanning the range $(0.4-2.5)\times10^5$ cm s^{-2} (Burrows et al. 1997), demonstrative gravity effects may be present.

As noted in § 4.3, the Color-e index (which measure the K I red wing) shows substantial scatter with optical spectral type for classes later than T_o2 (Figure 7d), while the combined CrH-a/H_2O index is reasonably monotonic over this region. Figure 9 compares the Color-e and CrH-a/H_2O indices for all of our telluric-calibrated spectra. The general trends with T_{eff} and gravity are noted at the bottom, derived by measuring the indices on the spectral models of Burrows et al. (2002a). For CrH-a/$H_2O \lesssim 0.7$ (SpT $\gtrsim T_o2$), there is a clear divergence in the Color-e values, with 2MASS 0937+2931 being the most significant outlier. The simplest explanation for this divergence is intrinsic scatter in the indices (i.e., due to poor signal-to-noise in some of the spectra). However, we note two suggestive trends. First, the four objects with Hα emission (including SDSS 0423−0414; Kirkpatrick et al. 2003) generally have steeper spectral slopes (larger Color-e) than other objects with similar CrH-a/H_2O values. Gizis et al. (2000) have noted that for late-type M and L field dwarfs, Hα emission is generally found amongst the older, and hence more massive, objects. If this relation follows through into the T dwarf regime, then we expect the active objects to have higher surface gravities, and therefore systematically larger Color-e ratios. Second, one object in our sample has an independent age, and hence gravity, determination, the companion T_n8/T_o7 Gliese 570D (Burgasser et al. 2000b). At 2–5 Gyr, this brown dwarf has a surface gravity of $(1–2)\times10^5$ cm s^{-2} (Geballe et al. 2001). Below this object is the $T_n7.5/T_o7$ 2MASS 1217−0311 (Burgasser et al. 1999), which Leggett et al. (2003) have suggested may be a low-gravity T dwarf based on its somewhat weaker CIA H_2 absorption. Again, the relative positions of these sources in Figure 9 are consistent with the expected trends. Independent age/gravity information (e.g., kinematics, companionship to well-studied stars, or cluster membership) or improved spectral models are clearly needed to verify and calibrate these possible trends. If verified, the use of these indices could potentially enable mass estimation of cool T dwarfs in the field.

5.3. *Comparison of Optical and Near-Infrared Classifications*

With the singular exception of SDSS 0423−0414, optical and near-infrared classifications for the T dwarfs studied here are remarkably consistent. This is somewhat surprising, given the competing temperature and gravity dependencies of defining H_2O and CH_4 bands (Burrows & Sharp 1999) and K I and Na I resonance line wings, the relatively weak gravity dependence of the optical Cs I lines (Lodders 1999), and the strong gravity dependence of CIA H_2 in the near-infrared (Borysow, Jørgensen, & Zheng 1997). The accord between the classifications may be the result of minimal variation in metallicity and gravity over the majority of our sample, with temperature being the most important discriminant. Such a case would imply that current T dwarf classification schemes are *de facto* temperature-based. However, as discussed above, there is a sufficiently broad range of possible surface gravities for the spectra in our sample to exhibit gravity-sensitive signatures. If we were in fact sampling the full possible range of surface gravities, then the agreement between the classifications would require that competing gravity and temperature effects compensate for each other amongst all of the optical and near-infrared diagnostic spectral features. In this case, T subtypes would not map directly onto a temperature scale. Therefore, there is a clear need to identify and calibrate unique gravity signatures in order to assess how well current classification schemes track T_{eff}.

The agreement between optical and near-infrared classifications for mid- and late-type T dwarfs also suggests that the possible causes for disagreements between late-type L and early-type T dwarf classifications – condensate cloud opacity and/or duplicity – are not important in the later spectral types. In general, T dwarf spectra and photometry are well-matched to models without condensate cloud opacity (Tsuji, Ohnaka, & Aoki 1996, 1999; Allard et al. 1996, 2001; Burrows et al. 1997; Ackerman & Marley 2001; Tsuji 2002, however, see Marley et al. 2002; Burrows et al. 2002a), although low-level near-infrared photometric (Enoch, Brown, & Burgasser 2003) and spectroscopic (Nakajima et al. 2000) variability, attributed to condensate clouds, has been observed in some T dwarfs. These time-dependent variations are typically quite small, however, and do not significantly change the overall spectromorphology (Nakajima et al. 2000). As for duplicity, late-type T dwarf doubles are not affected by the substantial redistribution of spectral flux that occurs across the L/T transition (Dahn et al. 2002), which allows a late-type L dwarf to dominate optical emission while its early-type T dwarf companion dominates near-infrared emission. This scenario may explain the presence of CH_4 at 2.2 μm in the L6.5 unequal-magnitude binary 2MASS 0920+3517AB (Kirkpatrick et al. 2000; Reid et al. 2001; Nakajima, Tsuji, & Yanagisawa 2001), as well as the classification discrepancy for SDSS 0423−0414 (Kirkpatrick et al. 2003). Indeed, both binaries in our sample, 2MASS 1225−2739AB and 2MASS 1534−2952AB (Burgasser et al. 2003b), have essentially identical optical and near-infrared types. These considerations suggest that optical/near-infrared classification discrepancies may be unique to the L/T transition, although additional examples of such transition objects must be discovered and observed to verify that this is the case.

6. SUMMARY

We have examined LRIS red optical spectra for a sample of T dwarfs. These spectra are largely dominated by pressure-broadened Na I and K I features, which are highly sensitive to temperature, gravity, and metallicity. Weaker lines of Cs I and Rb I are also present, and appear to follow the trends of current chemical equilibrium calculations. Molecular bands of H_2O, CaH, CrH, FeH, and possibly CH_4 are also present. Hα emission is seen in three objects, weakly in SDSS 1254−0122 and 2MASS 1047+2124, but strong in the active T dwarf 2MASS 1237+6526. None of the spectra exhibit the 6708 Å Li I line, consistent with chemical depletion of this atomic species for $T \lesssim 1500$ K. Trends in the observed strengths of these features have allowed us to define a classification scheme in the red optical, accurate to within one subclass. Tying our scheme to selected near-infrared spectral standards, we

are able to make a consistent comparison between optical and near-infrared types, and hence a critical examination of spectromorphologies in these two spectral regions. We find excellent agreement between these classifications with the singular exception of SDSS 0423−0414, discussed in detail in Kirkpatrick et al. (2003). This agreement suggests that either current classification schemes are largely temperature-based, or that temperature and gravity effects compensate for each other throughout the 0.6–2.5 μm region. Disentangling these physical parameters may be possible by comparing the strength of the K I red wing and the 9250 Å H_2O band. Both gravity and metallicity affects help explain the peculiar spectrum of 2MASS 0937+2931, which may be a old, massive, and slightly metal-poor thick disk or halo brown dwarf. Further astrometric data and improved spectral models may help to characterize this unique brown dwarf. Clearly, while very little of the total luminosity of T dwarfs is emitted shortward of 1 μm, there are an abundance of physical diagnostics present in this spectral region that can be used to more fully characterize these cool brown dwarfs.

We are grateful to our Keck Observing Assistants Joel Aycock, Julie Rivera, and Terry Stickel, and Instrument Specialists/Support Astronomers Paola Amico, Tom Bida, and Bob Goodrich for their assistance during the data acquisition; and to the NASA TAC for its allocation of time for this project. A. J. B. also acknowledges support provided by NASA through a Hubble fellowship grant from the Space Telescope Science Institute, which is operated by the Association of Universities for Research in Astronomy, Incorporated, under NASA contract NAS5-26555. J. D. K. acknowledges the support of the Jet Propulsion Laboratory, California Institute of Technology, which is operated under contract with the National Aeronautics and Space Administration. A. B. acknowledges funding through NASA grants NAG5-10760 and NAG5-10629. This publication makes use of data from the Two Micron All Sky Survey, which is a joint project of the University of Massachusetts and the Infrared Processing and Analysis Center, funded by the National Aeronautics and Space Administration and the National Science Foundation. 2MASS data were obtain through the NASA/IPAC Infrared Science Archive, which is operated by the Jet Propulsion Laboratory, California Institute of Technology, under contract with the National Aeronautics and Space Administration. Portions of the data presented herein were obtained at the W. M. Keck Observatory which is operated as a scientific partnership among the California Institute of Technology, the University of California, and the National Aeronautics and Space Administration. The Observatory was made possible by the generous financial support of the W. M. Keck Foundation. The authors wish to extend special thanks to those of Hawaiian ancestry on whose sacred mountain we are privileged to be guests.

REFERENCES

Ackerman, A. S., & Marley, M. S. 2001, ApJ, 556, 872
Allard, F., Hauschildt, P. H., Alexander, D. R., Tamanai, A., & Schweitzer, A. 2001, ApJ, 556, 357
Allard, F., Hauschildt, P. H., Baraffe, I., & Chabrier, G. 1996, ApJ, 465, L123
Anders, E., & Grevesse, N. 1989, Geo. Cosmo. Acta, 53, 197
Auman, J., Jr. 1967, ApJS, 14, 171
Berg, L. E., & Klynning, L. 1974, A&AS, 13, 325
Borysow, A., Jørgensen, U. G., & Zheng, C. 1997, A&A, 324, 185
Burgasser, A. J. 2002, Ph.D. Thesis, California Institute of Technology
Burgasser, A. J., Kirkpatrick, J. D., McElwain, M. W., Cutri, R. M., Burgasser, A. J., & Skrutskie, M. F. 2003a, AJ, 125, 850
Burgasser, A. J., Kirkpatrick, J. D., Reid, I. N., Brown, M. E., Miskey, C. L., & Gizis, J. E. 2003b, ApJ, 586, 512
Burgasser, A. J., Kirkpatrick, J. D., Reid, I. N., Liebert, J., Gizis, J. E., & Brown, M. E. 2000a, AJ, 120, 473
Burgasser, A. J., Liebert, J., Kirkpatrick, J. D., & Gizis, J. E. 2002a, AJ, 123, 2744
Burgasser, A. J., Marley, M. S., Ackerman, A. S., Saumon, D., Lodders, K., Dahn, C. C., Harris, H. C., & Kirkpatrick, J. D. 2002b, ApJ, 571, L151
Burgasser, A. J., et al. 1999, ApJ, 522, L65
—. 2000b, ApJ, 531, L57
—. 2000c, AJ, 120, 1100
—. 2002c, ApJ, 564, 421
—. 2003c, ApJ, submitted
Burrows, A., Burgasser, A. J., Kirkpatrick, J. D., Liebert, J., Milsom, J. A., Sudarsky, D., & Hubeny, I. 2002a, ApJ, 573, 394
Burrows, A., Ram, R. S., Bernath, P., Sharp, C. M., Milsom, J. A. 2002b, ApJ, 577, 986
Burrows, A., Marley, M. S., & Sharp, C. M. 2000, ApJ, 531, 438
Burrows, A., & Sharp, C. M. 1999, ApJ, 512, 843
Burrows, A., & Volobuyev, M. 2003, ApJ, 583, 985
Burrows, A., et al. 1997, ApJ, 491, 856
Chabrier, G., & Baraffe, I. 1997, A&A, 327, 1039
Cushing, M. C., Rayner, J. T., Davis, S. P., & Vacca, W. D. 2003, ApJ, 582, 1066
Dahn, C. C., et al. 2002, AJ, 124, 1170
Dick, K. A., & Fink, U. 1977, J. Quant. Spec. Radiat. Transf., 18, 433
Dulick, M., Bauschlicher, C. W., Jr., Burrows, A., Sharp, C. M., Ram, R. S., & Bernath, P. 2003, ApJ, submitted
Enoch, M. L., Brown, M. E., & Burgasser, A. J. 2003, AJ, submitted
Epchtein, N., et al. 1997, The Messenger, 87, 27
Geballe, T. R., Saumon, D., Leggett, S. K., Knapp, G. R., Marley, M. S., & Lodders, K. 2001, ApJ, 556, 373
Geballe, T. R., et al. 2002, ApJ, 564, 466
Gelino, C. R., Marley, M. S., Holtzman, J. A., Ackerman, A. S., & Lodders, K. 2002, ApJ, 577, 433
Gizis, J. E. 1997, AJ, 113, 806
Gizis, J. E., Monet, D. G., Reid, I. N., Kirkpatrick, J. D., Liebert, J., & Williams, R. 2000, AJ, 120, 1085
Golimowski, D. A., Burrows, C. S., Kulkarni, S. R., Oppenheimer, B. R., & Brukardt, R. A. 1998, AJ, 115, 2579
Griffith, C. A., & Yelle, R. V. 1999, ApJ, 519, L85
Hall, P. B. 2002a, ApJ, 564, L89
—. 2002b, ApJ, 580, L77
Hamuy, M., Suntzeff, N. B., Heathcote, S. R., Walker, A. R., Gigoux, P., & Phillips, M. M. 1994, PASP, 106, 566
Harris, H. C., et al. 2003, ApJ, in preparation
Hawley, S. L., Gizis, J. E., & Reid, I. N. 1996, AJ, 112, 2799
Kirkpatrick, J. D., Henry, T. J., & McCarthy, D. W., Jr. 1991, ApJS, 77, 417
Kirkpatrick, J. D., Reid, I. N., Liebert, J., Gizis, J. E., Burgasser, A. J., Monet, D. G., Dahn, C. C., Nelson, B., & Williams, R. J. 2000, AJ, 120, 447
Kirkpatrick, J. D., et al. 1999, ApJ, 519, 802
—. 2003, AJ, in preparation
Kleman, B., & Uhler, U. 1959, Can. J. Phys., 37, 537
Leggett, S. K., Golimowski, D. A., Fan, X., Geballe, T. R., & Knapp, G. R. 2003, in Proceedings of the 12th Cambridge Workshop on Cool Stars, Stellar Systems, and the Sun, ed. A. Brown, T. R. Ayres, & G. M. Harper (Boulder: Univ. Colorado Press), p. 120
Leggett, S. K., Toomey, D. W., Geballe, T. R., & Brown, R. H. 1999, ApJ, 517, L139
Leggett, S. K., et al. 2000, ApJ, 536, L35
Liebert, J., Kirkpatrick, J. D., Cruz, K. L, Reid, I. N., Burgasser, A. J., Tinney, C. G., & Gizis, J. E. 2003, AJ, 125, 343
Liebert, J., Reid, I. N., Burrows, A., Burgasser, A. J., Kirkpatrick, J. D., & Gizis, J. E. 2000, ApJ, 533, L155
Liebert, J., Wehrse, R., & Green, R. F. 1987, A&A, 175, 173
Lodders, K. 1999, ApJ, 519, 793
Marley, M. S., Seager, S., Saumon, D., Lodders, K., Ackerman, A. S., Freedman, R., & Fan, X. 2002, ApJ, 568, 335

Martín, E. L., Delfosee, X., Basri, G., Goldman, B., Forveille, T., & Zapatero Osorio, M. R. 1999, AJ, 118, 2466
Martin, E. L., Rebolo, R., & Zapatero Osorio, M. R. 1996, ApJ, 469, 706
McCook, G. P., & Sion, E. M. 1999, ApJS, 121, 1
Mohanty, S., Basri, G., Shu, F., Allard, F., & Chabrier, G. 2002, ApJ, 572, 469
Morgan, W. W., & Keenan, P. C. 1973, ARA&A, 11, 29
Nakajima, T., Oppenheimer, B. R., Kulkarni, S. R., Golimowski, D. A., Matthews, K., & Durrance, S. T. 1995, Nature, 378, 463
Nakajima, T., Tsuji, T., Tamura, M., & Yamashita, T. 2000, PASJ, 52, 87
Nakajima, T., Tsuji, T., & Yanagisawa, K. 2001, ApJ, 561, L119
Oke, J. B., et al. 1995, PASP, 107, 375
Oppenheimer, B. R., Kulkarni, S. R., Matthews, K., van Kerkwijk, M. H. 1998, ApJ, 502, 932
Oppenheimer, B. R., Kulkarni, S. R., Matthews, K., & Nakajima, T. 1995, Science, 270, 1478
Putney, A. 1997, ApJS, 112, 527
Reid, I. N., Burgasser, A. J., Cruz, K., Kirkpatrick, J. D., & Gizis, J. E. 2001, AJ, 121, 1710
Rothman, L. S., et al. 1998, JQSRT, 60, 665
Shultz, A. B., et al. 1998, ApJ, 492, L181
Skrutskie, M. F., et al. 1997, in The Impact of Large-Scale Near-IR Sky Surveys, ed. F. Garzon (Dordrecht: Kluwer), p. 25
Stevenson, C. C. 1994, MNRAS, 267, 904
Tsuji, T. 2002, ApJ, 575, 264
Tsuji, T., Ohnaka, K., & Aoki, W. 1996, A&A, 308, L29
Tsuji, T., Ohnaka, K., & Aoki, W. 1999, ApJ, 520, L119
Wiese, W. L., Smith, M. W., & Glennon, B. M. 1966, Atomic Transition Probabilities, Vol. 1. (Washington, D. C.: GPO)
Wing, R. F., Cohen, J., & Brault, J. W. 1977, ApJ, 216, 659
York, D. G., et al. 2000, AJ, 120, 1579

TABLE 1
LOG OF LRIS OBSERVATIONS.

Object[a] (1)	SpT NIR/Opt.[b] (2)	UT Date (3)	t_{int} (s) (4)	Airmass (5)	Telluric Cal. (6)	Type[c] (7)	Ref (8)
2MASS J04151954−0935066	T_n8/T_o8	2001 Feb 20	6000	1.20–1.38	WD 0413-074	DA4	1
2MASS J05591914−1404488	T_n5/T_o5	2000 Mar 5	3600	1.20–1.22	WD 0552-041	DC9	2
2MASS J07271824+1710012	T_n7/T_o8	2000 Mar 5	1800	1.00	WD 0747+073.1	DC9	1
2MASS J07554795+2212169	$T_n5:/T_o6$	2001 Feb 20	2400	1.13–1.19	SAO 79820	G0 V	1
2MASS J09373487+2931409	T_n6p/T_o7	2000 Mar 5	3600	1.01	(WD 0924+199)[d]	(DC5)[d]	1
2MASS J10475385+2124234	$T_n6.5/T_o7$	2001 Feb 20	4800	1.06–1.22	HD 93583	G0 V	3
2MASS J12171110−0311131	$T_n7.5/T_o7$	2000 Mar 5	1800	1.11–1.16	WD 1225-079	DZA5	3
2MASS J12255432−2739466AB	T_n6/T_o6	2000 Mar 5	3600	1.48–1.50	WD 1225-079	DZA5	3
2MASS J12373919+6526148	$T_n6.5/T_o7$	2000 Mar 5	1800	1.46			3
		2001 Feb 20	2400	1.49–1.52	SAO 15828	F8 V	3
SDSSp J125453.90−012247.4	T_n2/T_o2	2001 Feb 20	3600	1.08–1.13	HD 111942	G0 V	4
Gliese 570D	T_n8/T_o7	2000 Mar 5	3600	1.33–1.36	WD 1444-174	DC9	5
		2001 Feb 20	4800	1.08–1.13	HD 131878	G0 V	5
2MASS J15031961+2525196	$T_n5.5/T_o6$	2003 Jan 2	1200	1.35–1.40	BD+26 2652	G0	6
2MASS J15344984−2952274AB	$T_n5.5/T_o6$	2001 Feb 20	2400	1.58–1.63	HD 138874	F7 V	1

[a]2MASS Point Source Catalog source designations are given as "2MASS Jhhmmss[.]ss±ddmmss[.]s". The suffix conforms to IAU nomenclature convention and is the sexagesimal Right Ascension and declination at J2000 equinox.

[b]Near-infrared spectral types from Burgasser et al. (2002c); optical spectral types from Tables 6 and 7.

[c]White dwarf spectral types from McCook & Sion (1999) and references therein.

[d]A background F/G dwarf background may have actually been observed; see § 2.

References. — (1) Burgasser et al. (2002c); (2) Burgasser et al. (2000c); (3) Burgasser et al. (1999); (4) Leggett et al. (2000); (5) Burgasser et al. (2000b); (6) Burgasser et al. (2003a).

TABLE 2
RED OPTICAL FEATURES IN T DWARFS.

Feature (1)	λ (μm) (2)	Transition (3)	Ref. (4)
Na I	5890[a]	$3s\ ^2S_{1/2} - 3p\ ^2P_{3/2}$	1,2
Na I	5896[a]	$3s\ ^2S_{1/2} - 3p\ ^2P_{1/2}$	1,2
Hα	6563	$3d\ ^2D_{5/2} - 2p\ ^2P_{3/2}$	1
CaH	6750–7050	0-0 band of $A^2\Pi$-$X^2\Sigma$	3
K I	7665[a]	$4s\ ^2S_{1/2} - 4p\ ^2P_{3/2}$	1,2
K I	7699[a]	$4s\ ^2S_{1/2} - 4p\ ^2P_{1/2}$	1,2
Rb I	7800	$5s\ ^2S_{1/2} - 5p\ ^2P_{3/2,1/2}$	1
Rb I	7948	$5s\ ^2S_{1/2} - 5p\ ^2P_{3/2,1/2}$	1
CH_4	8800–9200	$4(\nu_1,\nu_3)$	4
Cs I	8521	$6s\ ^2S_{1/2} - 6p\ ^2P_{3/2}$	1
CrH	8611 bandhead	0-0 band of $A^6\Sigma^+$-$X^6\Sigma^+$	5
FeH	8692 bandhead	1-0 band of $A^4\Delta$-$X^4\Delta$	6
Cs I	8943	$6s\ ^2S_{1/2} - 6p\ ^2P_{1/2}$	1
H_2O	9250–9400	$3(\nu_1,\nu_3)$	7
H_2O	9450–9800	$2(\nu_1,\nu_3) + 2\nu_2$	7
FeH	9896 bandhead	0-0 band of $A^4\Delta$-$X^4\Delta$	6
CrH	9969 bandhead	0-1 band of $A^6\Sigma^+$-$X^6\Sigma^+$	5

[a]Pressure-broadened over > 1000 Å.

[b]Detection of this feature is ambiguous; see §3.2 and Figure 4.

References. — (1) Wiese, Smith, & Glennon (1966); (2) Burrows, Marley, & Sharp (2000); (3) Berg & Klynning (1974); (4) Dick & Fink (1977); (5) Kleman & Uhler (1959) (6) Wing, Cohen, & Brault (1977); (7) Auman (1967).

TABLE 3

CS I AND RB I PSEUDO-EQUIVALENT WIDTHS.

Object (1)	SpT NIR/Opt[a] (2)	8521 Å Cs I λ_c (Å) (3)	8521 Å Cs I pEW (Å) (4)	8943 Å Cs I λ_c (Å) (5)	8943 Å Cs I pEW (Å) (6)	7800 Å Rb I λ_c (Å) (7)	7800 Å Rb I pEW (Å) (8)	7948 Å Rb I λ_c (Å) (9)	7948 Å Rb I pEW (Å) (10)
SDSS 1254−0122	T_n2/T_o2	8520±2	7.4±0.1	8942±2	6.2±0.2	7810±70	6±3	7947±8	4.6±1.1
2MASS 0559−1404	T_n5/T_o5	8522±2	6.3±0.6	8945±2	6.0±0.8	7800±30	4.2±1.9	7950±6	9.4±1.4
2MASS 0755+2212	$T_n5:/T_o6$	8521±3	5.0±0.4	8944±2	5.9±0.5	...	< 12	...	< 3
2MASS 1503+2525	$T_n5.5/T_o6$	8519±2	5.9±0.2	8941±2	6.3±0.9	7800±30	10±2	7944±15	6±2
2MASS 1534−2952AB	$T_n5.5/T_o6$	8517±2	6.9±0.4	8940±2	6.2±0.2	...	< 30	7943±8	13±9
2MASS 1225−2739AB	T_n6/T_o6	8522±2	7.0±1.7	8944±2	7.1±0.8	...	< 16	...	< 14
2MASS 0937+2931	T_n6p/T_o7 p	8520±2	4.3±0.5	8942±2	6.3±0.7	...	...	7949±17	11±4
2MASS 1047+2124	$T_n6.5/T_o7$	8522±3	4.0±0.7	8944±2	6.1±1.3	...	...	...	< 4
2MASS 1237+6526[b]	$T_n6.5/T_o7$	...	< 13	...	< 6	...	...	...	< 13
		8520±3	6.3±0.8	8943±2	4.9±1.0	...	< 17	...	< 16
2MASS 0727+1710	T_n7/T_o8	8519±3	4.1±1.3	8943±2	6.2±1.5	...	< 40	7949±10	17±8
2MASS 1217−0311	$T_n7.5/T_o7$	8521±2	4.9±1.7	8944±2	3.7±1.7	...	< 12	...	< 10
Gliese 570D[b]	T_n8/T_o7	8519±2	3.6±1.1	8941±2	4±3	...	< 18	...	< 8
		8520±3	4.8±0.6	8944±2	5.2±0.9	...	< 5	7951±7	9±4
2MASS 0415−0935	T_n8/T_o8	8520±11	1.5±0.9	8944±3	3.9±1.5	...	< 15	7948±7	9±3

[a]Near-infrared spectral types from Burgasser et al. (2002c); optical spectral types from Tables 6 and 7.

[b]First set of values from epoch 2000 March 5 (UT), second set of values from epoch 2001 February 20 (UT).

TABLE 4
Hα EMISSION STRENGTHS.

Object (1)	SpT NIR/Opt[a] (2)	$f_{H\alpha}$ (10^{-18} ergs cm^{-2} s^{-1}) (3)	$\log L_{H\alpha}/L_{bol}$ (4)
SDSS 1254−0122	T_n2/T_o2	7.5±2.5	−5.8
2MASS 0559−1404	T_n5/T_o5	< 6.1	< −6.1
2MASS 0755+2212	$T_n5:/T_o6$	< 12	< −5.1
2MASS 1503+2525	$T_n5.5/T_o6$	< 9.6	< −5.5
2MASS 1534−2952AB	$T_n5.5/T_o6$	< 17	< −5.2
2MASS 1225−2739AB	T_n6/T_o6	< 6.7	< −5.4
2MASS 0937+2931	T_n6p/T_o7 p	< 3.9	< −6.0
2MASS 1047+2124	$T_n6.5/T_o7$	5.9±2.7	−5.4
2MASS 1237+6526[b]	$T_n6.5/T_o7$	29.0±2.8[c]	−4.6
		105.8±2.8[c]	−4.1
2MASS 0727+1710	T_n7/T_o8	< 3.6	< −5.7
2MASS 1217−0311	$T_n7.5/T_o7$	< 7.7	< −5.3
Gliese 570D[b]	T_n8/T_o7	< 6.5	< −5.3
		< 9.0	< −5.1
2MASS 0415−0935	T_n8/T_o8	< 7.9	< −5.4

[a]Near-infrared spectral types from Burgasser et al. (2002c); optical spectral types from Tables 6 and 7.

[b]First set of values from epoch 2000 March 5 (UT), second set of values from epoch 2001 February 20 (UT).

[c]See Burgasser et al. (2002a) for a discussion on the variability of the Hα line in 2MASS 1237+6526.

TABLE 5
T DWARF SPECTRAL RATIOS IN THE RED OPTICAL.

Diagnostic (1)	Numerator (Å)[a] (2)	Denominator (Å)[a] (3)	Feature Measured (4)	Ref. (5)
Cs-a	$\langle F_{8496.1-8506.1}\rangle+\langle F_{8536.1-8546.1}\rangle$	$2\times\langle F_{8516.1-8526.1}\rangle$	8521 Å Cs I	1
Cs-b	$\langle F_{8918.5-8928.5}\rangle+\langle F_{8958.3-8968.3}\rangle$	$2\times\langle F_{8938.5-8948.3}\rangle$	8943 Å Cs I	1
H_2O	$\int F_{9220-9240}$	$\int F_{9280-9300}$	9250 Å H_2O	2
CrH-a	$\int F_{8560-8600}$	$\int F_{8610-8650}$	8611 Å CrH	3
CrH-b	$\int F_{9855-9885}$	$\int F_{9970-10000}$	9969 Å CrH	2[b]
FeH-a	$\int F_{8560-8600}$	$\int F_{8685-8725}$	8692 Å FeH	3
FeH-b	$\int F_{9855-9885}$	$\int F_{9905-9935}$	9896 Å FeH	2[b]
Color-e	$\langle F_{9140-9240}\rangle$	$\langle F_{8400-8500}\rangle$	Spectral Slope	2

[a]⟨⟩ denotes average of flux density in range specified; ∫ denotes integrated flux in range specified.

[b]Modified from ratio defined by Martín et al. (1999).

References. — (1) Kirkpatrick et al. (1999); (2) This paper; (3) Martín et al. (1999).

TABLE 6
STANDARD SPECTRAL RATIO VALUES.

Object (1)	Opt SpT (2)	Cs-a (3)	CrH-a/H_2O (4)	FeH-b (5)	Color-e (6)	Ref (7)
2MASS 1632+1904	L8	1.70	1.02	1.11	1.88	1
SDSS 1254−0122[a]	T_o2	2.01	0.78	1.13	4.02	2,3
2MASS 0559−1404	T_o5	1.77	0.63	1.37	4.24	2
SDSS 1624+0029	T_o6	1.68	0.47	1.15	3.83	4
2MASS 0415−0935[a]	T_o8	1.19	0.25	0.94	4.20	2,3

[a]Measured from combined spectrum averaged over separate epochs.

References. — (1) Kirkpatrick et al. (1999); (2) This paper; (3) Kirkpatrick et al. (2003); (4) Burgasser et al. (2000a).

TABLE 7

LATE-TYPE L AND T DWARF SPECTRAL RATIO VALUES AND OPTICAL SPECTRAL TYPES.

Object (1)	Cs-a (2)	CrH-a/H_2O (3)	FeH-b (4)	Color-e (5)	Optical SpT[a] Indices (6)	Optical SpT[a] Visual (7)	NIR SpT[b] (8)	Ref (9)
SD 0423−0414[c]	1.95 (T_o2)	1.20 (< L8)	1.44 (< T_o5)	2.21 (L8)	L8:[d]	< L8[d]	T_n0	1
SD 0837−0000	1.80 (L8/T_o2)	0.89 (L8/T_o2)	0.90 (< T_o5)	3.35 (L8/T_o2)	$T_o0\pm2$	T_o2	T_n1	1
SD 1021−0304	1.98 (T_o2)	0.67 ($T_o2/5$)	1.37 (T_o5)	3.85 (> T_o2)	$T_o4\pm2$	T_o2	T_n3	1
2M 1503+2525	1.61 (T_o6)	0.50 (T_o6)	1.30 ($T_o5/6$)	4.75 (> T_o2)	T_o6	$T_o5/6$	$T_n5.5$	2
2M 1534−2952AB	1.70 (T_o6)	0.54 ($T_o5/6$)	1.38 (T_o5)	4.47 (> T_o2)	T_o6	$T_o5/6$	$T_n5.5$	2
2M 0755+2212	1.50 ($T_o6/8$)	0.52 ($T_o5/6$)	1.33 (T_o5)	3.78 (> T_o2)	T_o6	$T_o5/6$	$T_n5.5$:	2
2M 1225−2739AB	1.82 (T_o5)	0.41 (T_o6)	1.17 (T_o6)	4.28 (> T_o2)	T_o6	T_o6	T_n6	2
SD 1346−0031	1.43 ($T_o6/8$)	0.35 ($T_o6/8$)	1.01 ($T_o6/8$)	5.01 (> T_o2)	T_o7	$T_o6/8$	T_n6	3
2M 0937+2931	1.55 ($T_o6/8$)	0.38 ($T_o6/8$)	1.09 ($T_o6/8$)	5.99 (> T_o2)	T_o7	$T_o6/8$ p[e]	T_n6 p	2
2M 1047+2124	1.46 ($T_o6/8$)	0.37 ($T_o6/8$)	1.00 ($T_o6/8$)	4.41 (> T_o2)	T_o7	$T_o6/8$	$T_n6.5$	2
2M 1237+6526[a]	1.58 (T_o6)	0.37 ($T_o6/8$)	0.92 (T_o8)	4.93 (> T_o2)	T_o7	$T_o6/8$	$T_n6.5$	2,3
2M 0727+1710	1.28 (T_o8)	0.36 ($T_o6/8$)	0.92 (T_o8)	3.84 (> T_o2)	T_o8	$T_o6/8$	T_n7	2
2M 1217−0311	1.71 ($T_o5/6$)	0.34 ($T_o6/8$)	0.92 (T_o8)	3.77 (> T_o2)	T_o7	T_o8	$T_n7.5$	2
Gliese 570D[b]	1.48 ($T_o6/8$)	0.34 ($T_o6/8$)	0.87 (T_o8)	4.39 (> T_o2)	T_o7	T_o8	T_n8	1,2

[a]Optical spectral types quoted in the paper are those derived from the spectral indices.

[b]Near-infrared spectral types from Burgasser et al. (2002c) except for SDSS 0423−0414 (Geballe et al. 2002).

[c]Measured from combined spectrum averaged over separate epochs.

[d]Classified in the optical as L7.5 by Kirkpatrick et al. (2003).

[e]Slope of K I red wing significantly exceeds that of all T dwarf standards.

References. — (1) Kirkpatrick et al. (2003); (2) This paper; (3) Burgasser et al. (2000a).

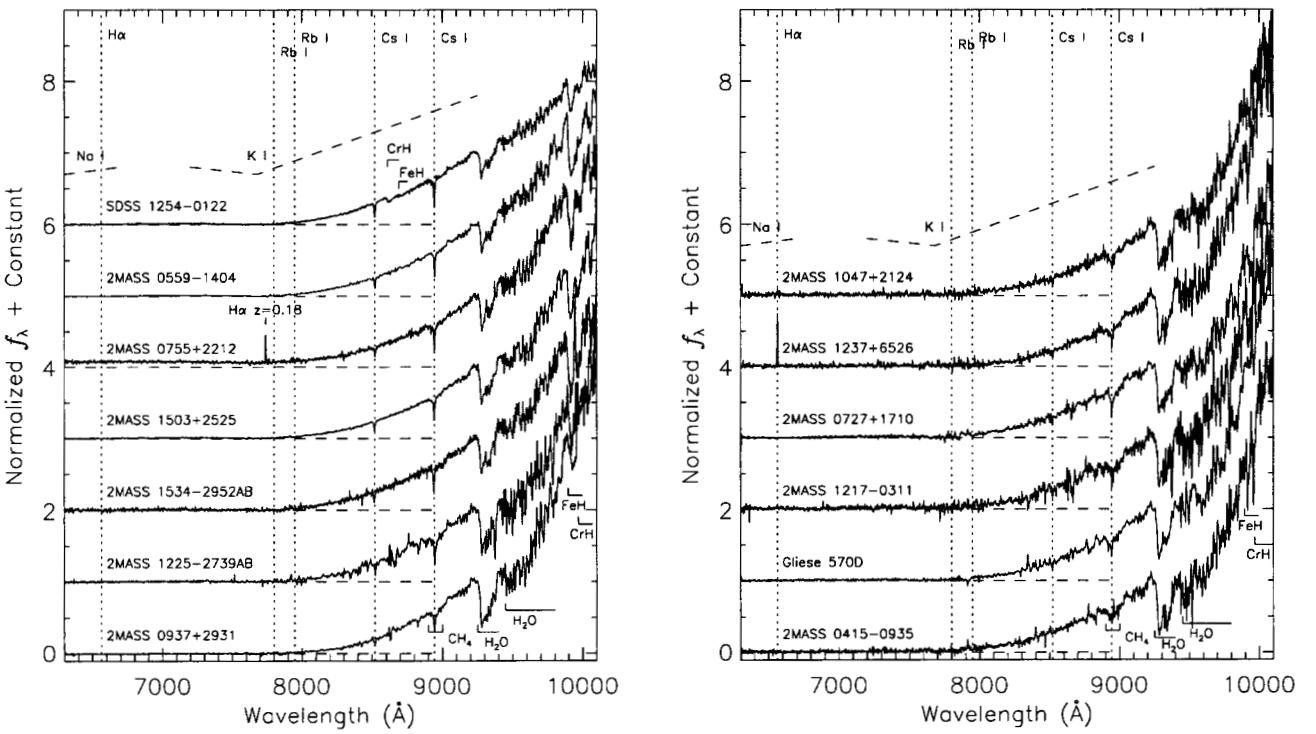

FIG. 1.— Reduced red optical (6300–10100 Å) spectra for our T dwarf sample. Data are normalized at 9250 Å and offset by a constant (dashed lines). Atomic and molecular absorption features listed in Table 2 are indicated. Note that the emission feature in the spectrum of 2MASS 0755+2212 is a redshifted ($z = 0.18$) Hα line from an aligned background galaxy.

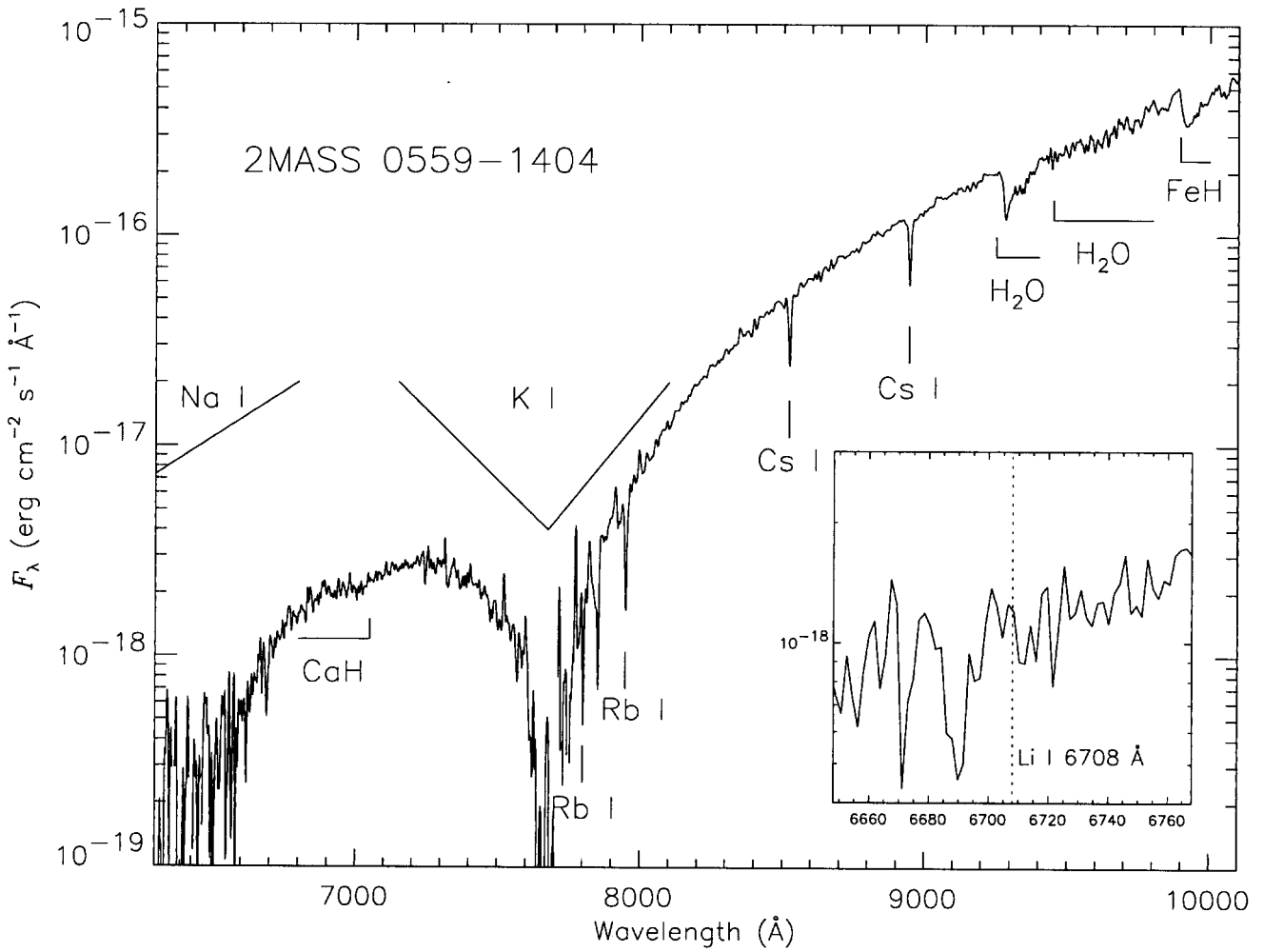

FIG. 2.— Spectrum of 2MASS 0559−1404, scaled to the flux density at 10 pc using I_c and parallax measurements from Dahn et al. (2002). Data are plotted on a logarithmic scale, and prominent spectral features are noted. The inset box shows a close-up of the 6650–6770 Å region around the 6708 Å Li I line. An offset feature is seen but is likely a noise spike; no obvious Li I line is detected.

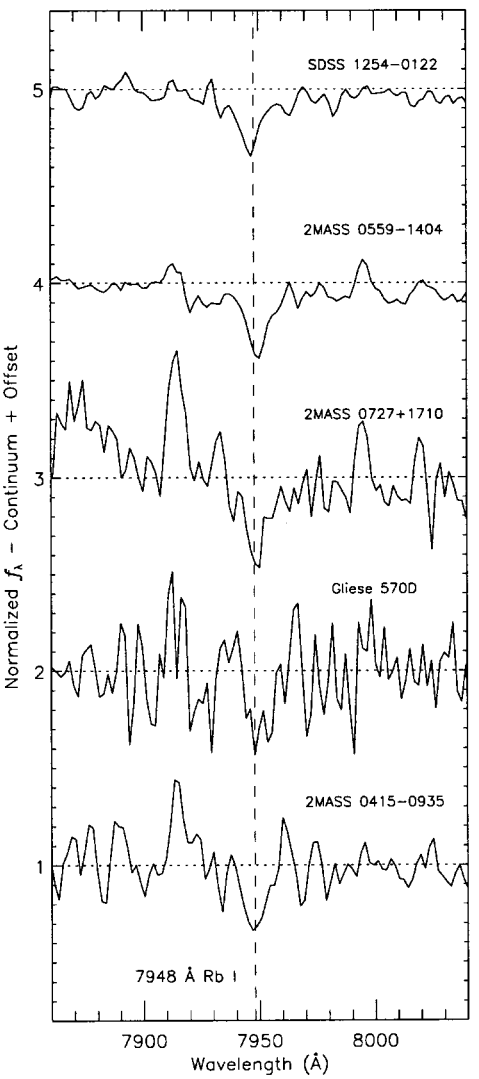

FIG. 3.— 7948 Å Rb I line (dashed vertical line) in the spectra of SDSS 1254−0122, 2MASS 0559−1404, 2MASS 0727+1710, Gliese 570D, and 2MASS 0415−0122. Spectra are normalized between 7900 and 8000 Å, and linear fits to the local pseudo-continua have been subtracted. Spectra are offset by a constant for clarity (dotted lines). Note that "emission features" at 7910 and 7990 Å are poorly-subtracted telluric OH skylines.

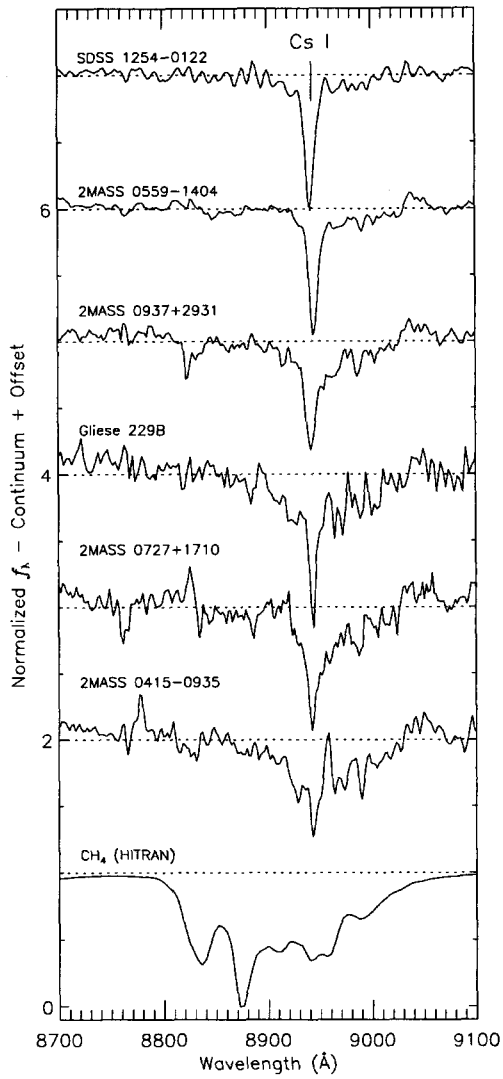

FIG. 4.— Close-up of the 8700–9100 Å region in the spectra of SDSS 1254−0122, 2MASS 0559−1404, 2MASS 0937+2931, Gliese 229B (data from Oppenheimer et al. 1998), 2MASS 0727+1710, and 2MASS 0415−0935. Spectra are normalized as in Figure 3. A normalized CH_4 opacity spectrum generated from data in the HITRAN database is plotted at the bottom for comparison. The 8943 Å Cs I line is also noted.

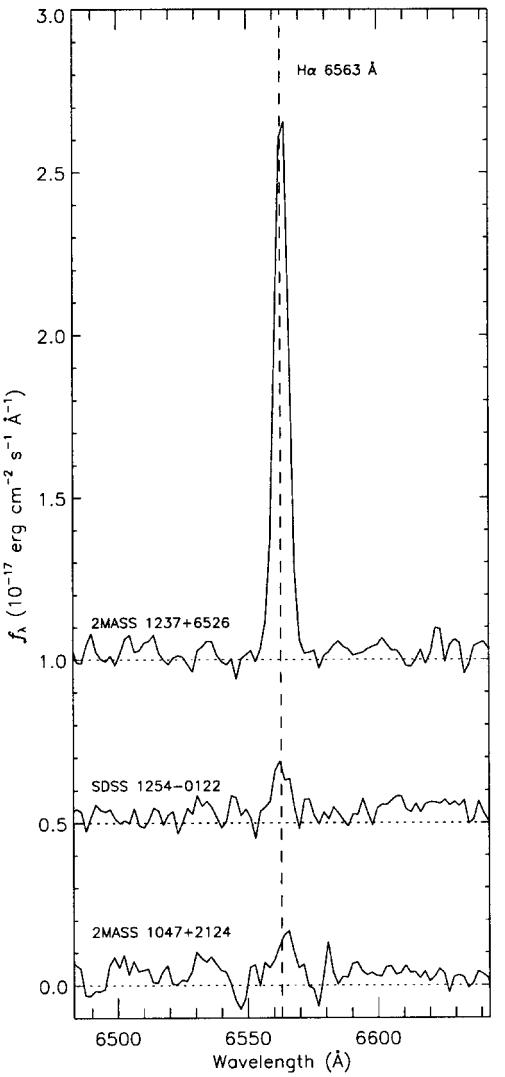

FIG. 5.— Spectral region around the 6563 Å Hα emission line (vertical dashed line) for 2MASS 1237+6526 (data from 2001 February 20 UT), SDSS 1254−0122, and 2MASS 1047+2124. Spectra are offset by a constant for clarity (dotted line).

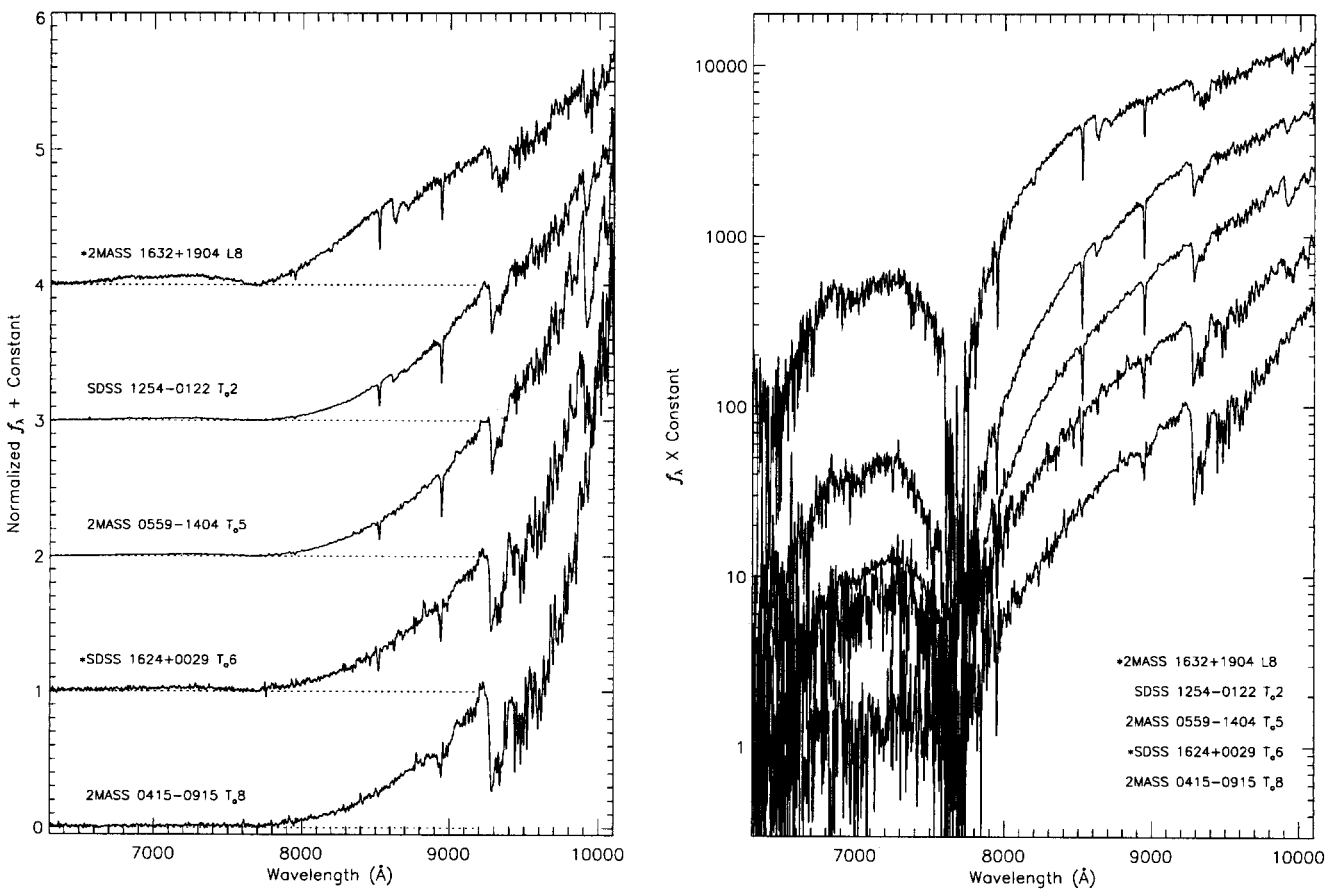

FIG. 6.— LRIS spectra of optical spectral standards 2MASS 1632+1904 (L8), SDSS 1254−0122 (T_o2), 2MASS 0559−1404 (T_o5), SDSS 1624+0029 (T_o6), and 2MASS 0415−0935 (T_o8). Spectra are normalized at 9250 Å. Objects labelled by an asterisk have not had their spectra corrected for telluric absorption. The left panel shows the standard spectra on a linear scale, offset by a constant; the right panel shows the spectra on a logarithmic scale, offset by a constant factor.

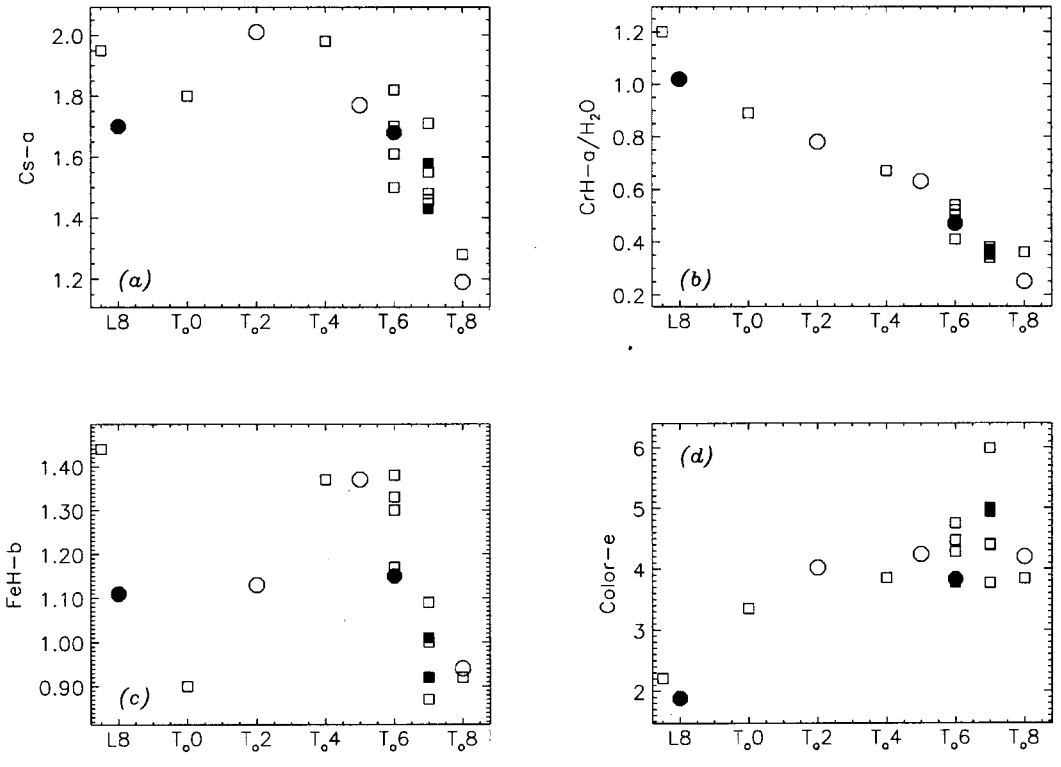

FIG. 7.— Spectral indices versus final optical spectral type (Table 7, column 6): (a) Cs-a, (b) CrH-a/H_2O, (c) FeH-b, and (d) Color-e. Spectral standards are indicated by circles, other spectra by squares. Spectra that have not been corrected for telluric absorption are indicated by filled symbols.

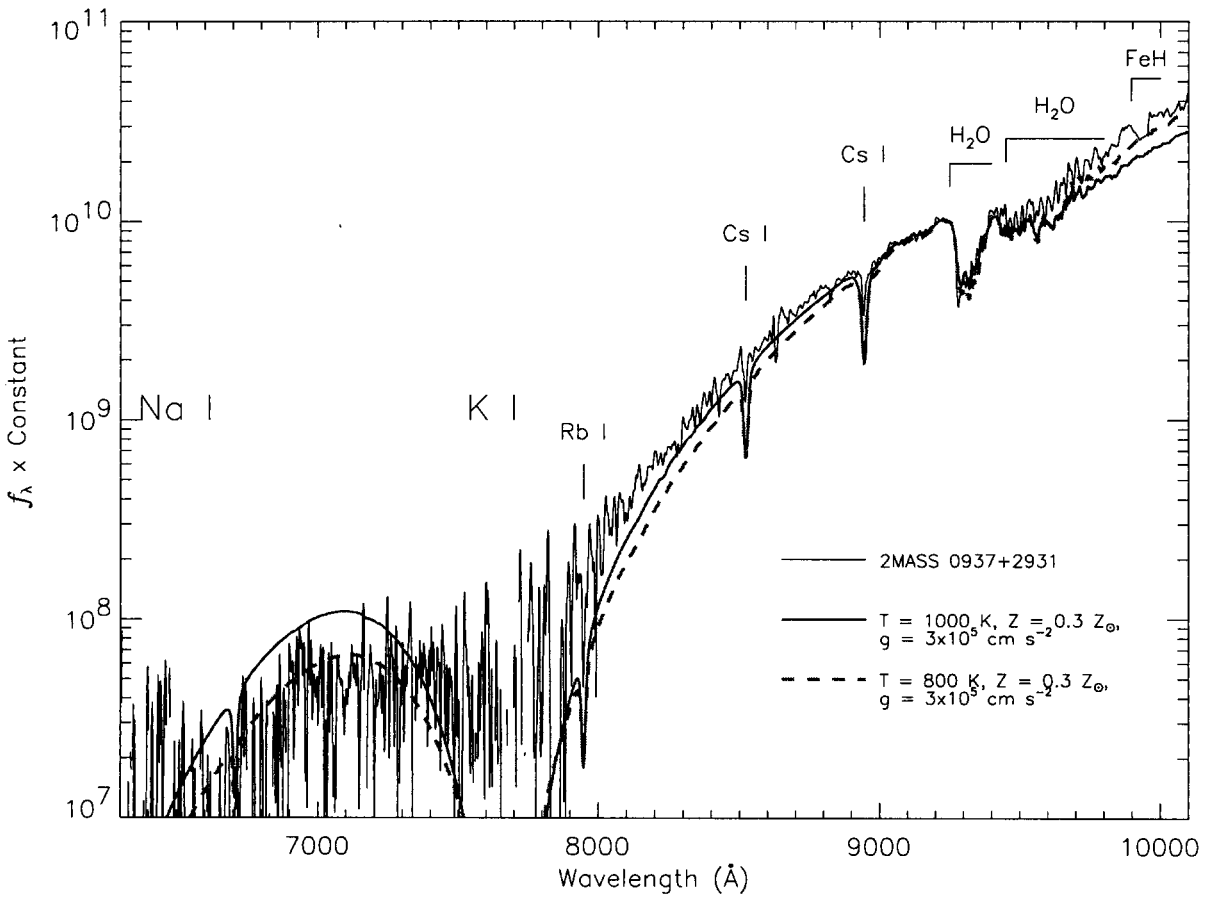

FIG. 8.— Spectral model fits to the peculiar T dwarf 2MASS 0937+2931. The best-fitting models from Burrows et al. (2002a) are shown, both with g = 3×10^5 cm s^{-2} and $Z = 0.3Z_\odot$, and having T_{eff} = 1000 (solid grey line) and 800 K (dashed grey line). Higher metallicity and/or lower gravity models do not match either the steep spectral slope over 8000–10000 Å or the suppression of flux at ~7100 Å between the broadened Na I and K I lines. Parallax measurement may provide a better constraint on the T_{eff} of this object.

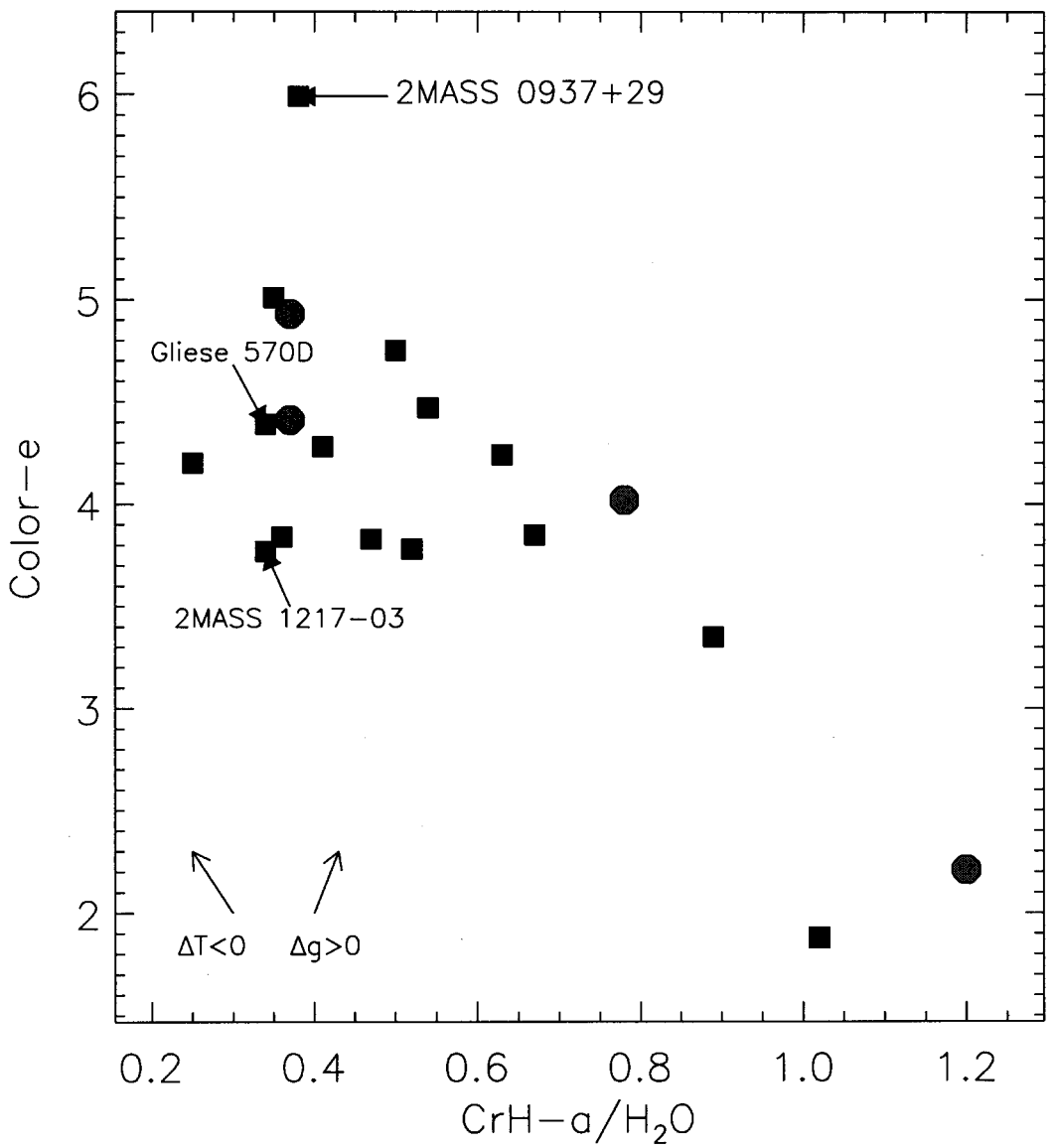

FIG. 9.— Color-e versus CrH-a/H_2O for our sample. Objects with Hα emission are indicated by circles, all others are indicated by squares. Three objects are labelled: the metal-poor T dwarf 2MASS 0937+2931, the moderate-gravity companion T dwarf Gliese 570D (Burgasser et al. 2000b; Geballe et al. 2001, τ = 2–5 Gyr, g = (1–2)$\times 10^5$ cm s^{-2}), and the possible low-gravity T dwarf 2MASS 1217−0311 (Leggett et al. 2003). General dependencies on decreasing temperature and increasing gravity at T_{eff} = 1000 K and $Z = Z_{\odot}$, based on the models of Burrows et al. (2002a), are indicated by the arrows in the lower left corner.